

# Tuning bacterial hydrodynamics with magnetic fields

C. J. Pierce,<sup>1</sup> E. Mumper,<sup>2</sup> E. E. Brown,<sup>2</sup> J. T. Brangham,<sup>1</sup> B. H. Lower,<sup>2</sup> S. K. Lower,<sup>2,3,4</sup> F. Y. Yang,<sup>1</sup> and R. Sooryakumar<sup>1,\*</sup>

<sup>1</sup>*Department of Physics, The Ohio State University, 191 W Woodruff Ave., Columbus, Ohio 43210, USA*

<sup>2</sup>*School of Environment and Natural Resources, The Ohio State University, 2021 Coffey Rd., Columbus, Ohio 43210, USA*

<sup>3</sup>*School of Earth Sciences, The Ohio State University, 125 Oval Dr. S, Columbus, Ohio 43210, USA*

<sup>4</sup>*Department of Microbial Infection and Immunity, The Ohio State University, 460 West 12th Ave., Columbus, Ohio 43210, USA*

(Received 2 July 2016; revised manuscript received 28 March 2017; published 30 June 2017)

Magnetotactic bacteria are a group of motile prokaryotes that synthesize chains of lipid-bound, magnetic nanoparticles called magnetosomes. This study exploits their innate magnetism to investigate previously unexplored facets of bacterial hydrodynamics at surfaces. Through use of weak, uniform, external magnetic fields and local, micromagnetic surface patterns, the relative strength of hydrodynamic, magnetic, and flagellar force components is tuned through magnetic control of the bacteria's orientation. The resulting swimming behaviors provide a means to experimentally determine hydrodynamic parameters and offer a high degree of control over large numbers of living microscopic entities. The implications of this controlled motion for studies of bacterial motility near surfaces and for micro- and nanotechnology are discussed.

DOI: [10.1103/PhysRevE.95.062612](https://doi.org/10.1103/PhysRevE.95.062612)

## I. INTRODUCTION

Low Reynolds number (Re) hydrodynamics [1], where viscous forces dominate inertial effects, is a fundamental feature of the movement of microscopic objects in fluids. This regime is also home to a staggering diversity of motile microorganisms, which have evolved mechanisms that produce directed movement in spite of viscous forces and Brownian motion. Such motility is typified by the swimming of bacteria, many of which rely on a slender helical attachment to their cell body, known as the flagellum, for propulsion. Flagella produce thrust at low Re through a nonreciprocal rotational motion which, as required by Purcell's scallop theorem [1], is noninvariant under time reversal.

In an unbounded fluid, the rotation of the flagellum produces a force on the cell body directed along its rotational axis, leading to movement at a constant velocity [2,3]. Near surfaces, however, more complex hydrodynamic forces and torques emerge [4–13], giving rise to a range of dynamical states that depend on the orientation of the cell relative to the surface, as well as its rotational velocity and cellular geometry. Understanding the hydrodynamic interactions of active swimmers, such as bacteria, at surfaces is important both in the study of swimming microorganisms, and also in the development of technologies that achieve controlled micromanipulation within fluidic environments.

In this study, a means of controlling microscopic motion and exploring surface-induced hydrodynamic interactions of a living organism, in the low Re regime, is presented. This is accomplished by exploiting the unique features of the motile and inherently magnetic bacterium, *Magnetospirillum magneticum* AMB-1, of the magnetotactic bacteria (MTB) group [14]. MTB dynamics are influenced by the forces arising from magnetic field gradients [15,16], while uniform external fields ( $H_{\text{ext}}$ ) allow control of the cell's orientation, and hence its direction of travel. Like all bacteria, they also experience effects of forces arising from the fluid itself. The

interplay between these magnetic and hydrodynamic effects has only begun to be explored [17]. We show that this magnetism reveals several aspects of bacterial hydrodynamics at surfaces which are inaccessible in nonmagnetic species such as the widely studied bacterium *Escherichia coli* [18]. Several interesting cases in which  $H_{\text{ext}}$  is used not only to direct cells along controlled paths through magnetic alignment, but also to tune the relative strength and/or orientation of hydrodynamic, flagellar, and magnetic field gradient forces at the surface are presented. This tunability produces a wide range of swimming behaviors: “toplike” and “orbitlike” states, linear trajectories that lie parallel or at constant angles to the paths of neighboring cells, and selective confinement and release of individual cells from specific trapping locations. Furthermore, the observed, magnetically tunable dynamics, allow for the quantitative determination of hydrodynamic parameters governing bacterial motility near surfaces. By allowing controlled and quantifiable magnetic forces to balance hydrodynamic forces of unknown strength, hydrodynamic models of surface-induced effects may be experimentally investigated in a systematic way.

Due to their high motility and ability to couple to external fields, MTB are also promising candidate microorganisms for biologically powered microactuation and robotics, both in artificial environments [19] and within the microvasculature of living organisms [20]. The linearity and reversibility of low Re fluid dynamics, a fundamental consequence of the scale of fluid borne microparticles, present both challenges and opportunities for robotics. The linearity of the dynamics makes control of objects via external forces, such as magnetism, more trivial than in the presence of inertial effects and the associated nonlinearities that emerge at larger length scales. Furthermore, because at sufficiently large field strengths (10–100 Oe) rotational diffusivity minimally affects the cell orientation, the trajectories of the cells are largely reversible. For example, by applying a series of oppositely sequenced external fields, the cells may be guided back to their initial positions. Alternatively, the dominance of viscous forces in this regime places restrictions on schemes for producing directed motion, particularly in the case of self-propulsion (swimming),

\*sooryakumar.1@osu.edu

which must result from motion which is noninvariant under time reversal [1]. However, MTB and other flagellated bacteria, through millennia of evolution, bear an efficient solution to this problem in the form of flagella, whose motion breaks time-reversal symmetry. Thus, MTB embody a set of valuable characteristics from the standpoint of actuation and robotics. Their innate magnetism offers a simple and flexible means of external control, allowing systematic exploration of the linear dynamics experienced in viscous environments. Moreover, unlike nonmotile, externally driven magnetic microparticles or many synthetic microswimmers, their well evolved approach to satisfying the constraints imposed by the linearity of the dynamics (the scallop theorem) yields a highly robust swimmer, capable of swimming at tens of body lengths per second.

## II. MATERIALS AND METHODS

The hydrodynamics and magnetic actuation possibilities of *M. magneticum* AMB-1 are observed and manipulated with a custom built system, used in previous studies of nonmotile magnetic microparticles [21–23]. In addition to uniform external fields ( $H_{\text{ext}} \approx 0\text{--}100$  Oe) from a three-axis electromagnet [21–23], linear segments ( $\mu\text{m}$  length) of 40-nm-thick ferromagnetic  $\text{Co}_{0.5}\text{Fe}_{0.5}$  patterns prepared via conventional photolithography give rise to “bar-magnet”-type domain structures, which produce large local field gradients ( $\approx 10^4$  T/m) at the surface [22]. A droplet of *M. magneticum* AMB-1 grown anaerobically in magnetic spirillum growth medium is confined at the surface in a 70- $\mu\text{m}$ -thick polydimethylsiloxane O-ring capped with a coverslip ( $\approx 100$   $\mu\text{m}$ ). The bacteria are imaged with a bright-field microscope in reflected mode. For single cell experiments, a 40 $\times$  or 63 $\times$  objective is used. For experiments involving large numbers of cells [e.g., Figs. 1(a), 4(b), and 4(c)], a wider field objective is used. Image analysis and trajectory tracking is done with IMAGEJ and MATLAB based protocols. For wide field experiments [e.g., Figs. 1(a), 4(b), and 4(c)], IMAGEJ is used to perform background subtraction, contrast enhancement, and finally  $k$ -space filtering to remove objects and optical artifacts that differ in size from the bacteria. Trajectories are then tracked and analyzed in MATLAB, using a modified version of the BACTRACK program developed by Berg’s group at Harvard University. To calculate the mean angle of a bacterial trajectory to the external field (Figs. 1 and 4), the four quadrant arctangent function ( $\text{atan2}$ ) is employed to avoid problems associated with calculating the mean of circular quantities.

## III. MAGNETOTACTIC BACTERIA

With a flagellum located at either end of their spiral shaped cellular envelope [Fig. 1(a), inset], *M. magneticum* AMB-1 can swim in the forward or reverse directions parallel to their long axes by changing the rotation direction of the flagella [24]. A chain of intracellular, membrane-bound magnetite nanoparticles (magnetosomes) in single domain states [25] lies parallel to the flagellar propulsion axis, lending it a permanent magnetic moment [Fig. 1(a), inset]. Consequently, cells swim along magnetic field lines when the magnetic interaction is adequately high to overcome rotational diffusivity and oxygen

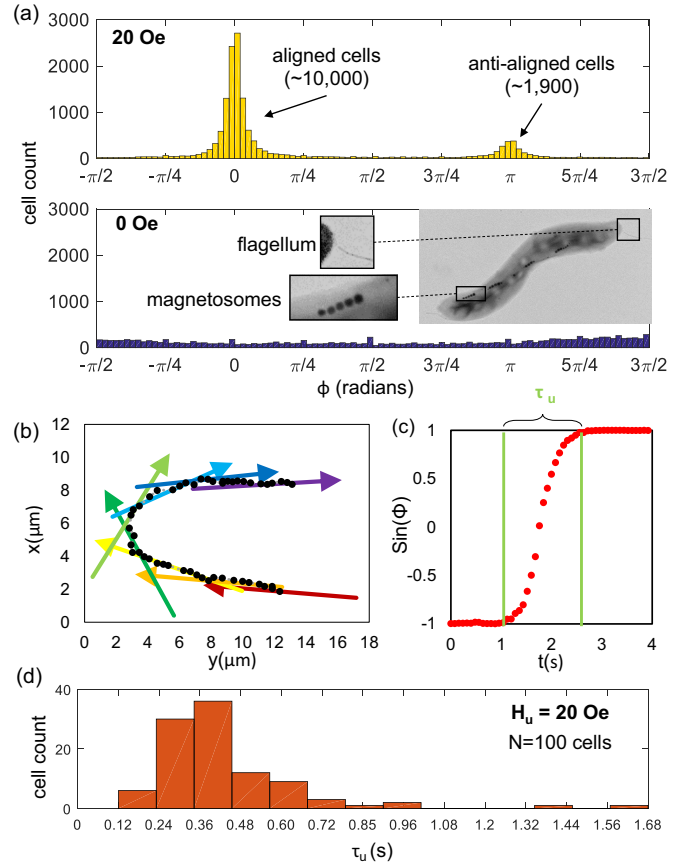


FIG. 1. (a) Histogram of cell orientations ( $\phi$ ) in the plane under magnetic fields oriented in the plane (at angle  $\phi = 0^\circ$ ; top, yellow) and in the absence of fields (bottom, blue). Inset: Transmission electron microscopy (TEM) image of *M. magneticum* AMB-1, with enlarged view of the flagellar attachment and a magnetosome chain. (b) Cell body orientation (arrows) and positions (points) during a typical U-turn experiment. As the field direction is rapidly reversed the cell takes a finite time  $\tau_u$  to turn. (c) Plot showing the sine of the cells’ orientation as a function of time under field reversal. The cell rotates by  $180^\circ$  in the green highlighted region. (d) Distribution of  $\tau_u$  for a collection of 100 cells.

or other stimulant concentrations are sufficiently controlled to suppress chemotactically regulated reversals of swimming direction [26]. Figure 1(a) (top), shows the distribution of cellular swimming orientations under an in-plane magnetic field (20 Oe) for a large number of cells ( $N \approx 15\,000$ ), taken from Supplemental Video s1 [27]. The large majority of cells ( $N \approx 10\,000$ ) are oriented parallel to the field, as seen in the large peak at 0 rad, while a smaller number of cells ( $N \approx 1900$ ) in a state of reversed flagellar polarity swim in the antiparallel direction ( $\pi$  rad). As expected, upon removal of the field, the cells rapidly assume random orientations [Fig. 1(b), bottom, and Supplemental Video s2 [27]].

In order to estimate the strength of the magnetic moment  $m$  of the cells, a U-turn method as described by Nadkarni *et al.* [28] is used. In this method, a cell is made to swim in a straight line path by an in-plane magnetic field ( $H_u$ ). The field is rapidly reversed, causing the cell to reorient [Fig. 1(b)]. Because of viscous drag forces on the cell, the bacteria require

a finite time ( $\tau_u$ ) to realign with the field [Fig. 1(c)], which depends on the relative strength of the magnetic interaction and the viscous forces. The experimentally observed turn time ( $\tau_u$ ) under rapid field direction reversal is related to the cell's magnetic moment ( $m$ ) by the following:

$$m = \frac{f_r}{\tau_u H_u}, \quad (1)$$

where we employ the rotational drag coefficient of a sphere  $f_r = 8\pi\eta r^3$  as a first approximation to the geometrically realistic drag coefficient of the spirochete cell envelope. Here,  $r$  is the equivalent sphere radius of the cell, and  $\eta$  the fluid viscosity.  $r$  is calculated using the experimental cell length  $L$ , determined by optical microscopy for each unique cell, and an estimate of the mean cell diameter ( $d \approx 500$  nm) determined from TEM. For the cell depicted in Figs. 1(b) and 1(c), this yields a value of  $m = (1.6 \pm 0.2) \times 10^{-16}$  A m<sup>2</sup>, a value typical of *M. magneticum* AMB-1 [28]. Figure 1(d) shows the distribution of U-turn times for a collection of 100 cells, collected in a wide field image, with an average  $\tau_u = 0.36$  s. Using the average value of the cell length from high magnification measurements ( $4.05 \mu\text{m}$ ), we can assign a mean magnetic moment of the collection as  $m = (2.0 \pm 0.8) \times 10^{-16}$  A m<sup>2</sup>. These experimental magnetic moments assume the drag coefficient  $f_r$  of a sphere, following previously reported studies [28]. While the correct drag coefficient for a rotating spirochete is nontrivial to calculate, a sphere represents an initial approximation. It is worth comparing, however, the values for a rod approximation (instead of a sphere). In this case, we have [29]

$$f_r = \frac{8\pi\eta d L^2}{3 \left[ \ln \left( \frac{2L}{d} \right) - \frac{1}{2} \right]}, \quad (2)$$

for which the calculated magnetic moment for the population in Fig. 1(d) is instead  $(9.6 \pm 3.8) \times 10^{-16}$  A m<sup>2</sup>. This increase in the magnetic moment is associated with the increase in the drag relative to the spherical case for the same aspect ratio. In reality, the true value of  $m$  likely lies between these two limiting cases.

#### IV. COMPETING HYDRODYNAMIC AND MAGNETIC TORQUES

We first consider a case in which  $H_{\text{ext}}$  is oriented perpendicular to a bare (nonmagnetic) surface [Figs. 2(a) and 2(b)]. Upon encountering the surface, the cells experience both a magnetic ( $L_M$ ) and a surface-induced, hydrodynamic ( $L_H$ ) torque [30] lying parallel to the surface plane. Interestingly, in contrast to the marine bacterium MO-1, AMB-1 does not display the “ping-pong” effect at the surface (wherein collisions with solid objects induce a reversal of swimming polarity) [31]. Tuning  $H_{\text{ext}}$  enables the relative magnitudes of  $L_M$  and  $L_H$  to be varied. For instance, control over  $L_M$  produces transitions between magnetically dominated “toplike” states, in which cells orient perpendicular to the surface and drift laterally in quasirandom walks (Fig. 3(a) right, [27]), and hydrodynamics-dominated states in which they align parallel to the surface, executing “orbitlike” circular trajectories [Fig. 3(a), left] [27] as observed with *E. coli* [32,33], despite differences in their respective flagellar arrangements. These latter circular

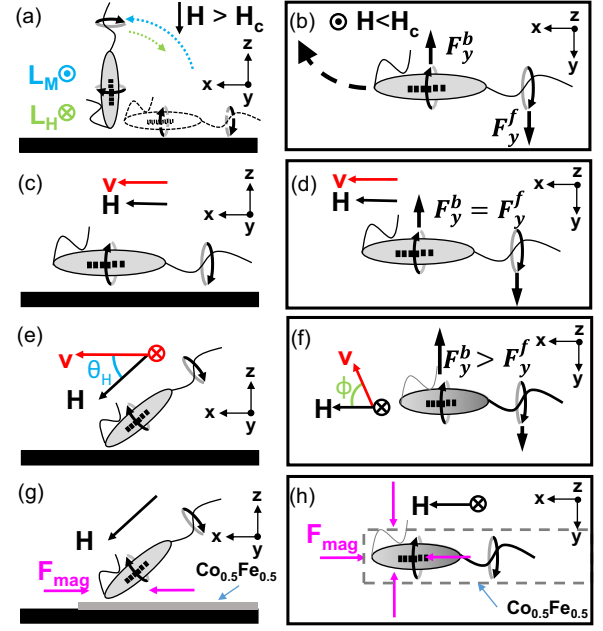


FIG. 2. (a) Competing hydrodynamic ( $L_H$ ) and magnetic ( $L_M$ ) torques control transitions between topline states (body in solid line) and planar states (body in dashed line) when  $H_{\text{ext}}$  is oriented perpendicular to the surface. (b) Rolling forces on the cell body  $F_y^b$  and flagellum  $F_y^f$  lead to circular swimming in the plane. (c, d) Cell swimming under purely in-plane field  $H_x$ , where  $F_y^b = F_y^f$ . (e, f) Cell oriented at an angle  $\theta_H$  relative to surface. (f) As cell is tilted out of plane,  $F_y^b$  is attenuated, yielding an unbalanced hydrodynamic force in the  $y$  direction, causing the bacterium to swim to the right of  $H_x$ . (g, h) Cell trapped by magnetic field gradient forces created by  $\text{Co}_{0.5}\text{Fe}_{0.5}$  micropatterns and oriented at an angle by the external field.

trajectories result from hydrodynamic rolling forces  $F_y^b$  and  $F_y^f$  on the counter-rotating body and leading flagellum ( $F_y^b$ ) and trailing flagellum ( $F_y^f$ ) that arise due to drag mismatch across the cell when in proximity to the surface [33]. As the flagellum propels the cell forward, the oppositely oriented roll forces cause the cell to swim in circular trajectories.

In order to quantitatively distinguish these two states, a single component of the cell velocity in both the time and frequency domain is considered. Figure 3(b) shows the power spectrum (blue) of a single velocity component taken along the horizontal axis of the recorded microscopy videos ( $v_x$ ) for a given cell, for a variety of field strengths. The corresponding time-domain curves are shown inset, in red. In the circular “orbitlike” trajectories that occur at lower field strengths, there are obvious periodicities observed in  $v_x$  that reflect the time scale of a full rotation [Fig. 3(b)]. In the “toplike” states, these periodicities are no longer present, as the motion is largely uncorrelated in time [Fig. 3(b)]. As evident in the 5 Oe trace [Fig. 3(b), bottom], fluctuations in the flagellar rotation rate, or cessations of motion, cause intermittent alignment of the cell body with the magnetic field, resulting from corresponding fluctuations in the strength of the hydrodynamic torque. These fluctuations in flagellar angular velocity arise both from stochastic effects as well as from the cell's ability

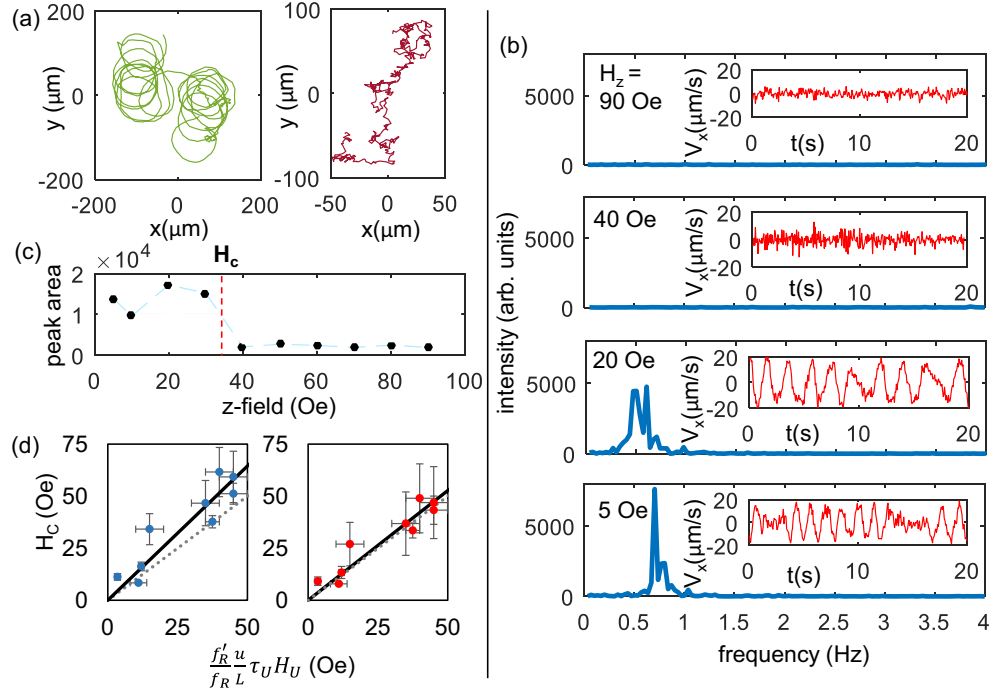


FIG. 3. (a) Left: At low field strength, hydrodynamic torques are dominant, causing the cell to execute circular motion in the plane. Right: As the out of plane field ( $H_z$ ) is increased, magnetic torques prevail and the cell orients perpendicular to the surface (toplike state), executing an uncorrelated random walk in the plane, as it rotates about its long axis. (b) Power spectra of the  $x$ -velocity component of an MTB trajectory under various  $z$ -field strengths (blue), with time domain velocities inset (red). (c) The peak area integrated from 0 to 1.5 Hz. Between  $H_z = 30$  and 40 Oe, the dramatic reduction in intensity represents the transition between the two states, allowing a critical field  $H_c$  to be assigned to the cell in question. (d) Left: theoretical vs experimental critical fields for multiple cells, based on simple scaling. Linear fit (solid line) indicates a prefactor of 1.29. Right: Theoretical vs experimental critical fields with corrections to the drag coefficient ratio in Eq. (5).

to biochemically regulate flagellar rotation. By observing the cell trajectories for extended time periods (minutes) the power spectrum of the  $x$ -velocity components are computed in order to determine which state (top- or orbitlike) the cell occupies at a given field strength. The change between the states is thus reflected in the power spectra by a decrease in the peaks associated with the period of the orbits. By plotting the area under the power spectrum over the region containing the peaks associated with the circular motion (0–1.5 Hz) for various field strengths, a critical field value ( $H_c$ ) beyond which circular motion is no longer observed can be defined [Fig. 3(c)]. Hence, a lower bound on the magnetic torque required to suppress the hydrodynamic torque experienced by the cell can be determined.

$H_c$  can be estimated by comparing the respective time scales of hydrodynamic ( $\tau_H$ ) [30] and magnetic ( $\tau_M$ ) reorientation. Here

$$\tau_H \approx \frac{L}{u} \quad \text{and} \quad \tau_M \approx \frac{f'_r}{m H_{\text{ext}}}, \quad (3)$$

where  $L$ ,  $u$ , and  $m$  are the cell's length, speed, and magnetic moment, respectively, and  $f'_r$  the out-of-plane rotational drag coefficient. The critical field occurs when these time scales are comparable and, thus, an estimate for  $H_c$  is

$$H_c = \frac{f'_r}{m} \frac{u}{L}. \quad (4)$$

For a given cell,  $u$  and  $L$  may be directly determined from the microscopy images, while  $m$  may be estimated using the U-turn method described above. Combining Eqs. (1) and (3), a scaling relationship for  $H_c$  in terms of the drag coefficients for rotations in the plane of the surface ( $f_r$ ) and out of the plane ( $f'_r$ ), as well as several measured parameters unique to each cell, is constructed:

$$H_c = \frac{f'_r}{f_r} \frac{u}{L} \tau_u H_u. \quad (5)$$

If the two drag coefficients ( $f'_r$ ,  $f_r$ ) are assumed to be comparable, Eq. (4) predicts a linear relationship between  $H_c$  and the product  $\frac{u}{L} \tau_u H_u$  with a slope of unity. However, a linear fit to the experimental values [shown in Fig. 3(d), left] shows that there exists a prefactor of 1.29. This scaling factor likely results from shape effects of the cell body, and also reflects differences between  $f_r$  and  $f'_r$ , which arise because of the presence of the surface. The drag coefficient for rotations about an axis normal to the plane ( $f_r$ ), which describes the drag force acting in the U-turn experiment, is expected to be smaller than  $f'_r$ , used to estimate the magnetic reorientation time scale ( $\tau_M$ ) in Eq. (2), which describes rotations about an axis lying in the surface plane.

As an initial estimate of the ratio of these drag coefficients, the corresponding mobilities calculated by Lauga *et al.* are employed [33] for a spheroid (ignoring the geometric details of spirochete cellular envelope). The mobilities associated with



each direction are similar apart from a logarithmic factor which takes into account the additional drag on objects rotating about an axis parallel to the surface plane. Thus, the ratio of the coefficients is approximately

$$\frac{f'_r}{f_r} = \frac{2}{5} \left[ \ln \left( \frac{r}{h} \right) + 0.38 \right], \quad (6)$$

where  $r$  is the cell's equivalent sphere radius [33] and  $h$  the size of the gap between the cell and the adjacent surface. While  $h$  may not be directly inferred from experiments, reasonable estimates of this value ( $h = 150$  nm; cf. [33]) account for the experimentally observed scaling factor well. Although this initial estimate ignores geometric details of the realistic cell shape, the logarithmic dependence of the correction on the ratio ( $r/h$ ) appears to correctly encapsulate the basic underlying physics. Approximating complex cell geometries as spherical objects greatly simplifies calculations. Furthermore, as the time scales of reorientation considered here are larger than a single cellular rotation, the torques considered effectively average over a number of cellular rotations, obscuring geometric details. Figure 3(d) (right), shows experimental data from nine cells scaled by the drag coefficient ratio in Eq. (5), using the appropriate, experimental equivalent sphere radius for each cell, and a gap height of  $h = 150$  nm. The experimental agreement with Eq. (4) [Fig. 3(d), right] confirms that the observed transition is a result of the interplay between hydrodynamic and magnetic torques.

The observed critical field ( $H_c$ ), taken along with the experimentally determined magnetic moment ( $m$ ) for each cell, permits direct calculation of the magnetic torque at the critical field, and hence provides an estimate of the hydrodynamic torque responsible for pulling the cells into the planar orientation ( $L_H$ ):

$$L_H \approx L_M \approx m H_c \approx \frac{f_r H_c}{\tau_u H_u}. \quad (7)$$

Using  $f_r = 8\pi\eta r^3$ , where  $\eta$  is the fluid viscosity and  $r$  the cell's equivalent sphere radius [33], we estimate an average magnetic moment of the cells represented in Fig. 3(d) as  $(2.0 \pm 1.6) \times 10^{-16}$  A m<sup>2</sup>, similar to previously reported values [28]. Using these measured magnetic moments for each cell, along with the experimentally observed  $H_c$ , we present the first direct measurement of  $L_H$  as  $0.45 \pm 0.17$  pN  $\mu$ m, averaged for the group of cells analyzed in Fig. 3(d). Although its strength may vary, this torque influences the motion of any hydrodynamically analogous flagellated swimmer near solid surfaces [30]. This technique, achieved through the exploitation of the innate magnetism of this model species, can serve as a foundation for further exploration of this and other hydrodynamic surface torques and forces.

## V. TUNING HYDRODYNAMIC FORCES FOR NONPARALLEL MULTICELL MANIPULATION

Next, several field geometries are discussed under which tunable magnetic and hydrodynamic surface interactions offer unique means of manipulating cellular positions. These states offer control over the motion of multiple cells in deterministic yet nonparallel ways. The resulting dynamical states have profound implications for biology-driven microrobotics and

actuation. Under purely in-plane ( $H_x$ ) external fields, MTB swimming near surfaces are stabilized in a planar orientation by both hydrodynamic [30] and magnetic forces. In contrast, as discussed above for perpendicular fields ( $H_z$ ), the hydrodynamic and magnetic torques compete. Above a threshold field value of  $H_x$ , the bacteria swim parallel to the field and one another [Figs. 2(c) and 2(d)], as the magnetic torque counters the hydrodynamic torque that results from the “rolling” forces on the body ( $F_y^b$ ) and flagellum ( $F_y^f$ ). The observed alignment of bacterial velocities with  $H_{\text{ext}}$  [Figs. 1(a) and 4(b)] suggests the two rolling forces ( $F_y^b, F_y^f$ ) are of comparable magnitude.

Alternatively, external fields with both in-plane ( $H_x$ ) and out-of-plane ( $H_z$ ) components tilt the cell body away from the surface [Figs. 1(e) and 1(f)], altering the parallel swimming achieved with purely planar fields. In this case the propelling flagellum is tilted away from the plane, thereby reducing  $F_y^f$  as the drag mismatch is correspondingly attenuated as the flagellum is taken away from the surface. Since the front of the cell body and leading flagellum remain in near contact with the surface,  $F_y^b$  is now unmatched by  $F_y^f$  on the trailing flagellum, causing the cell to move perpetually to the right [viewed from above; Fig. 2(f)]. Thus, although the tilted cell body remains aligned with the net field, its center-of-mass velocity is directed at an angle  $\phi$  relative to  $H_x$  and the cell's long axis, as shown in Fig. 2(f).

In general, surface-induced hydrodynamic forces depend on a given cell's unique rotation rate and detailed geometrical characteristics, which vary considerably from cell to cell. Variation of micro-object parameters has been previously explored as a route toward nonparallel manipulation of multiple objects, through design of object geometries which exhibit unique responses to external stimuli [34]. Here, we instead rely on the inherent variations of properties from cell to cell to achieve controlled nonparallel motion. As illustrated in Fig. 4(a), this inherent variability in bacterial parameters within a population enables controlled differentiation of individual cellular trajectories. As an out-of-plane field component  $H_z$  is supplied,  $F_y^f$  is attenuated to a different degree for each cell, thereby causing cells to turn rightward by differing amounts, depending on the cell length, flagellar thrust, and magnetic moment. Figure 4(a) shows two trajectories collected from neighboring cells, illustrating transitions between parallel swimming under purely in-plane field and nonparallel trajectories through tilted magnetic fields. Since at field strengths under consideration (90 Oe) rotational diffusion is small on experimental time scales, these trajectories are largely reversible. Upon reversal of the “magnetic instructions” imposed upon the cell, the cells may be guided back to their initial positions. Moreover, for a given cell at a particular tilt angle, the angle of the turn ( $\phi$ ) executed upon imposition of an  $H_z$  is observed to remain constant over time [27] for a particular cell.

Figure 4 illustrates the veer angle ( $\phi$ ) for a large group of cells under purely in-plane field conditions [Fig. 4(b)], as well as under a field tilted at an angle of  $80^\circ$  [Fig. 4(c)], plotted as a function of the in-plane velocity. Under purely in-plane fields a large portion of the cells align with the field to the extent allowed by rotational diffusivity. In addition, the bacterial culture considered here displays a relatively large,

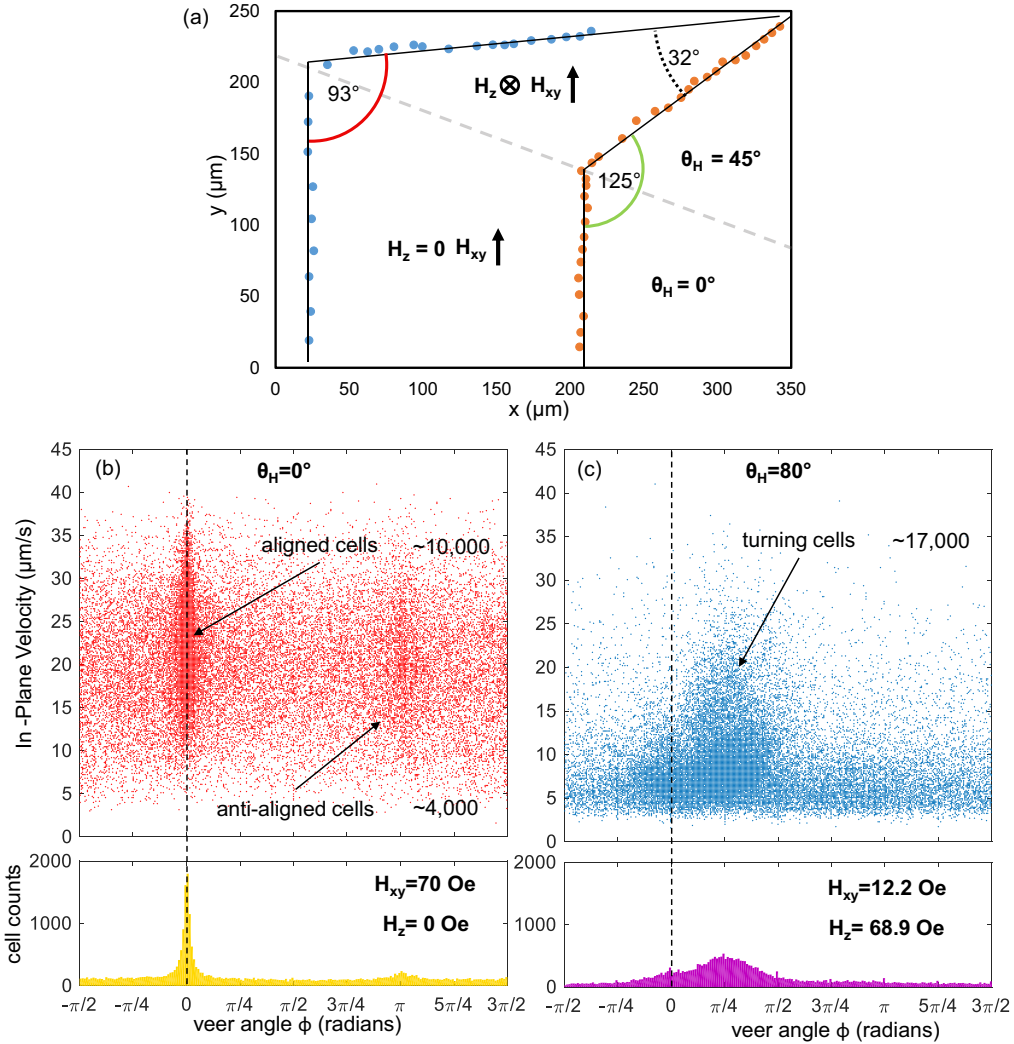


FIG. 4. (a) Trajectories of two cells in an external field ( $H_{\text{ext}} = 90$  Oe). Cells begin swimming (bottom left) with  $H_z = 0$  ( $\theta_H = 0$ ), along parallel paths. When the  $z$  field is turned on, the net field is tilted out of plane ( $\theta_H = 45^\circ$ ) and both cells turn rightward by different amounts, causing their trajectories to differ by a constant angle of  $32^\circ$ . Swimming velocity vs veer angle  $\phi$  for cells under purely in-plane fields (b) and fields tilted  $80^\circ$  out of the plane (c). The panels on the bottom show the corresponding cell number as a function of  $\phi$ . The dramatically reduced velocity results from projecting the propulsive force out of the plane yet constraining the cell to remain in the plane.

randomly aligned background signal, associated with cells with immature magnetism (compared, for example, with the culture displayed in Fig. 1). As the field is tilted, the density of angles near alignment extends broadly, reaching to a range of nearly  $90^\circ$  [Fig. 4(c)], as  $f_y^b$  is no longer counteracted by  $f_y^f$ . Furthermore, as the cell's flagellar orientation is now dramatically altered, the propulsive force no longer lies purely in the plane, leading to reduced in-plane velocities. Moreover, additional resistive forces are experienced by the cell as it drives itself into the surface, further reducing the velocities. To determine the number of cells in the aligned and antialigned peaks, histograms are integrated in the region of the peak, using a half width of  $\pi/8$  for the in-plane case [Fig. 4(b)]. The number of cells assumed to be turning [Fig. 4(c)] is estimated by integrating from  $-\pi/4$  to  $\pi/2$ . In both experiments, the total number of cells is comparable ( $N \approx 30\,000$ ). While one may expect the total number of cells associated with turning ( $N \approx 17\,000$ ) to be comparable to that of the aligned cells

( $N \approx 10\,000$ ), we instead observe an apparent discrepancy. This is likely a consequence of the difficulty of conserving the total cell number in a given field of view. Due to spatial inhomogeneities in the cell density, as the cells continuously swim out of the field of view, their number is, in general, not constant. To minimize the effect, for a given tilt angle  $\theta_H$ , the in-plane field is reversed after each recorded video, shifting the cells back to their approximate initial conditions. Furthermore, the introduction of cells from the bulk fluid to the image plane under tilted fields tends to increase the number of cells in the turning state. Additionally, antialigned cells are guided to the top surface of the fluid cell and outside of the depth of focus of the image. The phenomena of magnetically tilted cells at surfaces thus reveals a mechanism by which cells may be induced to swim along paths at a variety of angles relative to one another. This mechanism allows a single parameter, the external field, to direct the motion of multiple microscopic entities along both parallel and nonparallel,

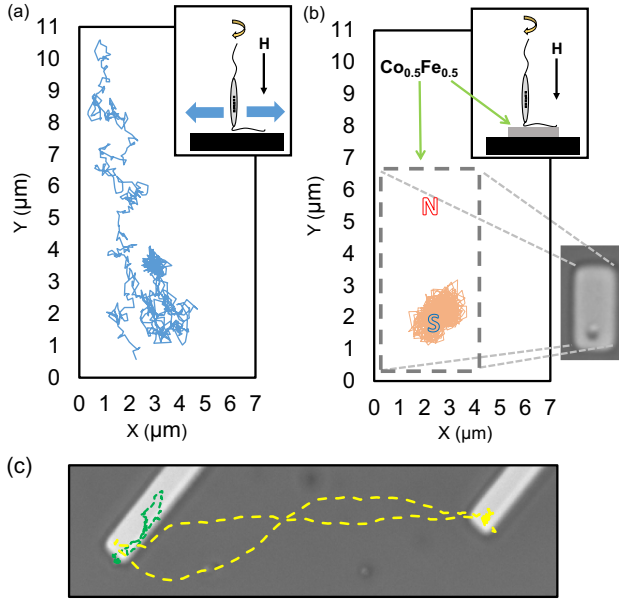


FIG. 5. (a) A two-dimensional quasirandom walk of a topleike bacterium above a bare (nonmagnetic) surface. (b) Trajectory of the same cell in (a) above a  $\text{Co}_{0.5}\text{Fe}_{0.5}$  micro bar magnet. The magnetic forces oriented toward the “south” pole (S) of the bar suppress the cell’s lateral fluctuations, resulting in confinement for arbitrary lengths of time. (c) Round trip trajectory of the two cells near a pair of magnetic wires. A sequence of fields guides a cell off the initial trap to a neighboring trap and back (yellow trajectory). Another cell (green trajectory) deviates from the center of the trap at the wire’s end, but insufficient flagellar force is projected into the plane to cause the cell to escape the wire trap.

deterministic paths. Such a level of control will be of significance in the creation of bacterial microrobotics and assembly platforms.

## VI. BACTERIAL CATCH AND RELEASE

The inclusion of micromagnetic surface patterns provides an additional means by which the two forces (flagellar and magnetic gradient) affecting bacterial dynamics may be tuned. A bacterium encountering a “bar magnet”-type domain [22] experiences repulsion at the “north” (N) terminus while a “south” (S) end creates an attractive potential energy trap [22] which suppresses the cell’s lateral positional fluctuations [23] through forces on the magnetosome chain. Thus, the cell can be confined without physical tethering within a small region ( $\mu\text{m}^2$ ) for long time periods (hours). As illustrated in Figs. 5(a) and 5(b) and the supplemental video [27], reversible and nonlethal localization of a highly motile organism is achieved.

In the presence of a constant  $H_z$  with a bacterium confined to the south pole trap [Figs. 2(g) and 2(h)], an increasing in-plane field,  $H_x$ , tilts the cell body towards the surface. As the orientation of the cell body deviates from verticality, an increasing component of the flagellar propulsion force  $F_f$  is projected onto the surface plane which, at a critical angle  $\Theta_C$ , becomes comparable to the in-plane confinement force from the south trap. For  $\theta_H > \Theta_C$ ,  $F_f$  enables the bacterium to escape the trap.  $\Theta_C$  depends on the bacterial

magnetic moment  $m$  as well as the flagellar propulsion force  $F_f$ . Since  $F_f$  and  $m$  vary across a cell population,  $\Theta_C$  is unique to a given cell, permitting the selective removal from confinement of individual cells within a population. This selective separation is illustrated for two bacteria in Fig. 5(c) and the supplemental video [27] wherein one bacterium is removed from a domain wall trap, moved to another, and returned to its original position while the other remains in the vicinity of the first trap. Furthermore, the onset of escape provides for a reliable estimate of the flagellar force to be  $\approx 2 \pm 0.8$  pN ( $F_f \approx F_{\text{mag}} \approx 2m \frac{dH}{dx} \approx 2 \times 10^{-16}$  A  $\text{m}^2 \times 10^4$  T/m), a value in good agreement with previous optical tweezers-based measurements of flagellar forces [35,36].

## VII. CONCLUSION AND OUTLOOK

Bacteria, and microorganisms in general, can be regarded as self-replicating machines that direct chemical synthesis, growth, and movement in response to diverse physical stimuli. In this light, the intersection of the study of living matter and the central technological problem of dynamically actuating functional materials of microscopic dimensions becomes apparent. While such observations have inspired biomimetic approaches to micromanipulation [37–41], synthetic implementations of biomimetic principles seldom approach the level of complexity exhibited by actual living systems. In describing the various means of magnetic and hydrodynamic control over MTB at surfaces we move beyond biomimetics, extending the possibilities of microactuation through direct exploitation of bacterial physiology in biohybrid systems [42]. Their unique magnetic sensitivity, nontrivial hydrodynamics, and the inherent variability of physical properties within the population have, as discussed, led to novel means of control and actuation in the microscopic regime.

In summary we have exploited the unique characteristics of MTB to tune bacterial hydrodynamics near solid surfaces with weak magnetic fields. These results demonstrate an alternative approach to investigating the surface-induced hydrodynamics of active swimmers. In this regard, we have successfully provided direct experimental determination of the hydrodynamic torque responsible for the accumulation of swimmers near surfaces [30], and a direct measurement of flagellar thrust. By controlling hydrodynamic, flagellar, and magnetic forces, previously unreported MTB trajectories have been observed. Furthermore, by exploiting the inherent variations of magnetic and flagellar properties across a cellular population, individual trajectories of multiple microorganisms can be independently directed along nonparallel paths via a single parameter, the external field  $H_{\text{ext}}$ , and through the use of micromagnetic traps, captured and released on a selective basis. This ability to control multiple objects in both parallel and nonparallel ways and to programmatically halt individual objects is central to realizing functional microrobotic technologies. The control mechanisms identified in this work, when combined with schemes to controllably functionalize the cells, (i.e., carrying cargo with useful chemical, mechanical, electronic, or optical properties), could serve as the basis for a variety of novel, dynamic, microscale machines operating in low Re environments.

## ACKNOWLEDGMENTS

This work was supported in part by the U.S. Army Research Office under Contract No. W911NF-14-1-0289 and the NSF Grants No. EAR-1424138, No. DMR-1420451, and

No. DMR-1507274. We also thank Zachery Oestreicher for TEM Images, and Tianyu Yuan for assistance with data collection.

- [1] E. Purcell, *Am. J. Phys.* **45**, 3 (1977).
- [2] E. Lauga and T. R. Powers, *Rep. Prog. Phys.* **72**, 096601 (2009).
- [3] E. Lauga, *Annu. Rev. Fluid Mech.* **48**, 105 (2016).
- [4] D. Lopez and E. Lauga, *Phys. Fluids* **26**, 071902 (2014).
- [5] L. Lemelle, J. Palierne, E. Chatre, and C. Place, *J. Bacteriol.* **192**, 6307 (2010).
- [6] D. Giacché, T. Ishikawa, and T. Yamaguchi, *Phys. Rev. E* **82**, 056309 (2010).
- [7] M. A. Vieant, R. M. Ford, M. Wagner, and L. K. Tamm, *Appl. Environ. Microbiol.* **68**, 2794 (2002).
- [8] A. Petroff, X. Wu, and A. Libchaber, *Phys. Rev. Lett.* **114**, 158102 (2015).
- [9] H. Wioland, F. G. Woodhouse, J. Dunkel, J. O. Kessler, and R. E. Goldstein, *Phys. Rev. Lett.* **110**, 268102 (2013).
- [10] B. Misselwitz, N. Barrett, S. Kreibich, P. Vonaesch, D. Andrichke, S. Rout, K. Weidner, M. Sormaz, P. Songhet, P. Horvath, M. Chabria, V. Vogel, D. M. Spori, P. Jenny, and W.-D. Hardt, *PLoS Pathog.* **8**, e1002810 (2012).
- [11] R. Nosrati, A. Driouchi, C. M. Yip, and D. Sinton, *Nat. Commun.* **6**, 8703 (2015).
- [12] M. Edwards, R. Carlsen, and M. Sitti, *Appl. Phys. Lett.* **102**, 143701 (2013).
- [13] H. Shum and E. A. Gaffney, *Phys. Rev. E* **91**, 033012 (2015).
- [14] C. Lefevre and D. Bazylinski, *Microbiol. Mol. Biol. Rev.* **77**, 497 (2013).
- [15] L. M. González, W. C. Ruder, P. R. Leduc, and W. C. Messner, *Sci. Rep.* **4**, 4104 (2014).
- [16] J. Loehr, D. Pfeiffer, D. Schuler, and T. Fischer, *Soft Matter* **12**, 3631 (2016).
- [17] N. Waisbord, C. T. Lefèvre, L. Bocquet, C. Ybert, and C. Cottin-Bizonne, *Phys. Rev. Fluids* **1**, 053203 (2016).
- [18] H. C. Berg, *E. Coli in Motion* (Springer, New York, 2004).
- [19] S. Martel, C. Tremblay, S. Ngakeng, and G. Langlois, *Appl. Phys. Lett.* **89**, 233904 (2006).
- [20] O. Felfoul, M. Mohammadi, S. Taherkani, D. de Lanauze, Y. Xu, D. Loghin, S. Essa, S. Jancik, D. Houle, M. Lafleur, L. Gaboury, M. Tabrizian, N. Kauo, M. Atkin, T. Vuong, G. Batists, N. Beuchemin, D. Radzioch, and S. Martel, *Nat. Nanotechnol.* **11**, 941 (2016).
- [21] T. Henighan, A. Chen, G. Vieira, A. J. Hauser, F. Yang, J. Chalmers, and R. Sooryakumar, *Biophys. J.* **98**, 412 (2010).
- [22] G. Vieira, T. Henighan, A. Chen, A. J. Hauser, F. Y. Yang, J. J. Chalmers, and R. Sooryakumar, *Phys. Rev. Lett.* **103**, 128101 (2009).
- [23] A. Chen, G. Vieira, T. Henighan, M. Howdyshe, J. A. North, A. J. Hauser, F. Y. Yang, M. G. Poirier, C. Jayaprakash, and R. Sooryakumar, *Phys. Rev. Lett.* **107**, 087206 (2011).
- [24] D. Murat, M. Herisse, L. Espinosa, A. Bossa, F. Alberto, and L. Wu, *J. Bacteriol.* **197**, 3275 (2015).
- [25] D. Bazylinski and R. Frankel, *Nat. Rev. Microbiol.* **2**, 217 (2004).
- [26] C. Lefevre, M. Bennet, L. Landau, P. Vach, D. Bazylinski, R. Frankel, S. Klumpp, and D. Faivre, *Biophys. J.* **107**, 527 (2014).
- [27] See Supplemental Material at <http://link.aps.org/supplemental/10.1103/PhysRevE.95.062612> for wide-field video microscopy of cells under a uniform in-plane field; cells swimming in zero field; video of a cell in a toplike state; video of cell in an orbitlike state; video of a cell trapped at a micromagnetic trap; and video of two cells independently controlled using micromagnetic traps to differentiate their motion.
- [28] R. Nadkarni, S. Barkley, and C. Fradin, *PLoS One* **8**, e82064 (2014).
- [29] H. C. Berg, *Random Walks in Biology* (Princeton University Press, Princeton, NJ, 1983), pp. 81–85.
- [30] A. P. Berke, L. Turner, H. C. Berg, and E. Lauga, *Phys. Rev. Lett.* **101**, 038102 (2008).
- [31] S. Zhang, N. Peterson, W. Zhang, S. Cargou, J. Ruan, D. Murat, C. Santini, T. Song, T. Kato, P. Notareschi, Y. Li, K. Namba, A. Gue, and L. Wu, *Environ. Microbiol. Rep.* **6**, 14 (2014).
- [32] H. Berg and L. Turner, *Biophys. J.* **58**, 919 (1990).
- [33] E. Lauga, W. DiLuzio, G. Whitesides, and H. Stone, *Biophys. J.* **90**, 400 (2006).
- [34] E. Diller, S. Floyd, C. Pawashe, and M. Sitti, *IEEE Trans. Robotics* **28**, 172 (2011).
- [35] S. Chattopadhyay, R. Moldovan, C. Yeung, and X. Wu, *Proc. Natl. Acad. Sci. USA* **103**, 13712 (2006).
- [36] N. C. Darnton, L. Turner, S. Rojevsky, and H. C. Berg, *J. Bacteriol.* **189**, 1756 (2006).
- [37] S. Palagi, A. Mark, S. Y. Reigh, K. Melde, T. Qiu, H. Zeng, C. Parmeggiani, D. Martella, A. Sanchez-Castillo, N. Kapernaum, F. Giesselmann, D. Wiersma, E. Lauga, and P. Fischer, *Nat. Mater.* **15**, 647 (2016).
- [38] W. Gao, X. Feng, A. Pei, C. R. Kane, R. Tam, C. Hennessy, and J. Wang, *Nano Lett.* **14**, 305 (2014).
- [39] R. Dreyfus, J. Baudry, M. Roper, M. Fermigier, H. Stone, and J. Bibette, *Nature* **437**, 862 (2005).
- [40] A. M. Maier, C. Weig, P. Oswald, E. Frey, P. Fischer, and T. Liedl, *Nano Lett.* **16**, 906 (2016).
- [41] L. Zhang, K. Peyer, and B. J. Nelson, *Lab on a Chip* **10**, 2203 (2010).
- [42] J. Zhuang, R. W. Carlsen, and M. Sitti, *Sci. Rep.* **5**, 11403 (2015).